

Unexpected spin-crossover at low temperature and low pressure, in an iron(II)/dipyrazolylpyridine complex exhibiting a high-spin Jahn-Teller distortion

Laurence J. Kershaw Cook[†], Flora L. Thorp-Greenwood[†], Tim P. Comyn[¶], Oscar Cespedes,[§]

Guillaume Chastanet^{‡} and Malcolm A. Halcrow^{*†}*

[†]School of Chemistry, University of Leeds, Woodhouse Lane, Leeds LS2 9JT, UK.

[¶]Institute for Materials Research, School of Process, Environmental and Materials Engineering, University of Leeds, Leeds LS2 9JT, UK.

[§]School of Physics and Astronomy, University of Leeds, E. C. Stoner Building, Leeds LS2 9JT, UK.

[‡]CNRS, Université de Bordeaux, ICMCB, UPR 9048, F-33600 Pessac, France.

Supporting Information

Definitions of the structural distortion parameters discussed in the paper.

Table S1 Selected bond lengths and angles in the crystal structures of **1**·4MeNO₂ and **2**·4MeNO₂.

Table S2 Selected bond lengths and angles in the crystal structures of solvent-free **2** and **3**.

Figure S1 Two view of the packing diagram of **1**·4MeNO₂, showing the channels of anions and solvent running parallel to *c*.

Figure S2 Packing diagram of **2**, showing a side-on view of the terpyridine embrace layers in the lattice.

Table S3 Metric parameters for the intermolecular π - π interactions in the terpyridine embrace layers in **2**.

Figure S3 Differential scanning calorimetry (DSC) trace of **1**.

Figure S4 Variable temperature X-ray powder patterns from **1** at 10-20 Torr pressure.

Figure S5 Variable temperature X-ray powder patterns from **2** at 10-20 Torr pressure.

Figure S6 Comparison of the high-spin structure of **2**, with the overlaid high-spin and low-spin molecular structures of **5** and **6**.

Table S4 Structural changes taking place during spin-crossover for [Fe(1-bpp)₂]²⁺ and its derivatives, whose high-spin and low-spin crystal structures are available.

Chart S1 Ligands referred to in Table S4.

Figure S7 Plots of $T_{1/2}$ for solid [Fe(1-bpp)₂]²⁺ derivatives against the distortion parameters θ , ϕ , Σ and Θ of the high-spin state of the complexes.

Figure S8 Relationship between $T_{1/2}$ and $T(\text{LIESST})$ for compounds from the [Fe(1-bpp)₂]²⁺ series, measured by these authors.

Figure S9 Variable temperature magnetic susceptibility data for **3** and **4**·½H₂O.

References

Definitions of the structural parameters discussed in the paper.

The Jahn-Teller distortion parameters ϕ and θ are shown in Chart 1 of the main article.

α is the average of the four internal *cis*-N–Fe–N angles within the two chelate ligands, which increases from *ca.* 73° in the high-spin state to 80° in the low-spin state.

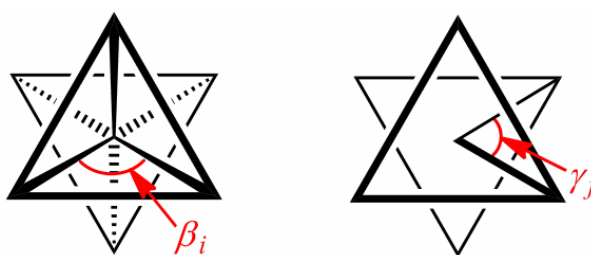
Σ and Θ are defined as follows:

$$\Sigma = \sum_{i=1}^{12} |90 - \beta_i| \qquad \Theta = \sum_{j=1}^{24} |60 - \gamma_j|$$

where β_i are the twelve *cis*-N–Fe–N angles about the iron atom and γ_j are the 24 unique N–Fe–N angles measured on the projection of two triangular faces of the octahedron along their common pseudo-threefold axis (Scheme S1). Σ is a general measure of the deviation of a metal ion from an ideal octahedral geometry, while Θ more specifically indicates its distortion towards a trigonal prismatic structure. A perfectly octahedral complex gives $\Sigma = \Theta = 0$.

Σ and Θ were originally introduced to quantify small differences in the coordination geometries of high-spin iron(II) complexes of polydentate ligands.¹ More recently, they were popularized by Guionneau *et al.* as a way of confirming the spin state of a metal ion in a crystal structure; and to quantify the magnitude of the structural changes taking place during spin-crossover through $\Delta\Sigma$ and $\Delta\Theta$, the differences in these parameters between the high- and low-spin states of the complex.²

Because the high-spin state of a complex has a much more plastic structure than the low-spin, this is reflected in Σ and Θ which are usually much larger in the high-spin state. The absolute values of these parameters depend on the metal/ligand combination in the compound under investigation, however.³ Typical values for these parameters for $[\text{Fe}(\text{bpp})_2]^{2+}$ complexes are tabulated in ref. 4.



Scheme S1. Angles used in the definitions of the coordination distortion parameters Σ and Θ .

Σ and Θ (and $\Delta\Sigma$ and $\Delta\Theta$) are measures of the change in the metal ion coordination sphere between the spin states. In contrast, ϕ and θ (and $\Delta\phi$ and $\Delta\theta$) quantify the change in shape of the molecule as a whole during spin-crossover, by describing the disposition of the organic ligands with respect to each other.

Table S1 Selected bond lengths and angles in the crystal structures of **1**·4MeNO₂ and **2**·4MeNO₂ (Å, °). See Fig. 2 of the main article for the atom numbering scheme employed. Symmetry codes: (i) $\frac{3}{2}-x, 2-z$; (ii) $2-x, 1-y, z$; (iii) $\frac{1}{2}+y, -\frac{1}{2}+x, 2-z$.

	1 ·4MeNO ₂	2 ·4MeNO ₂
Fe(1)–N(2)	1.894(5)	1.894(2)
Fe(1)–N(7)	1.981(5)	1.971(2)
N(2)–Fe(1)–N(7)	79.78(13)	80.05(6)
N(2)–Fe(1)–N(2 ⁱⁱ) (ϕ)	180	180
N(2)–Fe(1)–N(7 ⁱⁱ)	100.22(12)	99.95(6)
N(7)–Fe(1)–N(7 ⁱ)	159.6(2)	160.11(11)
N(7)–Fe(1)–N(7 ⁱⁱ)	91.7(3)	92.15(12)
N(7)–Fe(1)–N(7 ⁱⁱⁱ)	92.0(3)	91.27(12)
θ	90	90

Table S2 Selected bond lengths and angles in the crystal structures of solvent-free **2** and **3** (Å, °). See Fig. 2 of the main article for the atom numbering scheme employed. Symmetry code: (iv) $-x, y, \frac{1}{2}-z$.

2	100 K	240 K	3	
Fe(1)–N(2)	2.1236(19)	2.126(6)	Fe(1)–N(2)	2.1479(15)
Fe(1)–N(9)	2.1735(19)	2.182(7)	Fe(1)–N(9)	2.1774(16)
Fe(1)–N(14)	2.1893(19)	2.182(7)	Fe(1)–N(14)	2.1877(16)
Fe(1)–N(19)	2.1354(19)	2.137(6)		
Fe(1)–N(26)	2.2417(19)	2.241(7)		
Fe(1)–N(31)	2.1642(18)	2.159(6)		
N(2)–Fe(1)–N(9)	73.76(7)	74.1(2)	N(2)–Fe(1)–N(9)	72.88(6)
N(2)–Fe(1)–N(14)	73.36(7)	73.6(2)	N(2)–Fe(1)–N(14)	72.57(6)
N(2)–Fe(1)–N(19) (ϕ)	160.06(7)	163.7(2)	N(2)–Fe(1)–N(2 ^{iv}) (ϕ)	157.92(9)
N(2)–Fe(1)–N(26)	88.55(7)	91.7(3)	N(2)–Fe(1)–N(9 ^{iv})	91.03(6)
N(2)–Fe(1)–N(31)	124.92(7)	121.7(2)	N(2)–Fe(1)–N(14 ^{iv})	125.17(6)
N(9)–Fe(1)–N(14)	146.70(7)	147.3(3)	N(9)–Fe(1)–N(14)	143.75(6)
N(9)–Fe(1)–N(19)	112.53(7)	109.4(3)		
N(9)–Fe(1)–N(26)	95.02(7)	93.7(3)	N(9)–Fe(1)–N(9 ^{iv})	87.60(9)
N(9)–Fe(1)–N(31)	99.74(7)	99.0(3)	N(9)–Fe(1)–N(14 ^{iv})	103.63(6)
N(14)–Fe(1)–N(19)	100.25(7)	103.0(3)		
N(14)–Fe(1)–N(26)	89.27(7)	91.8(3)		
N(14)–Fe(1)–N(31)	94.70(7)	94.0(3)	N(14)–Fe(1)–N(14 ^{iv})	87.58(9)
N(19)–Fe(1)–N(26)	72.29(7)	72.3(3)		
N(19)–Fe(1)–N(31)	73.79(7)	74.1(2)		
N(26)–Fe(1)–N(31)	146.02(7)	146.4(3)		
θ	89.62(2)	89.48(7)	θ	67.70(2)

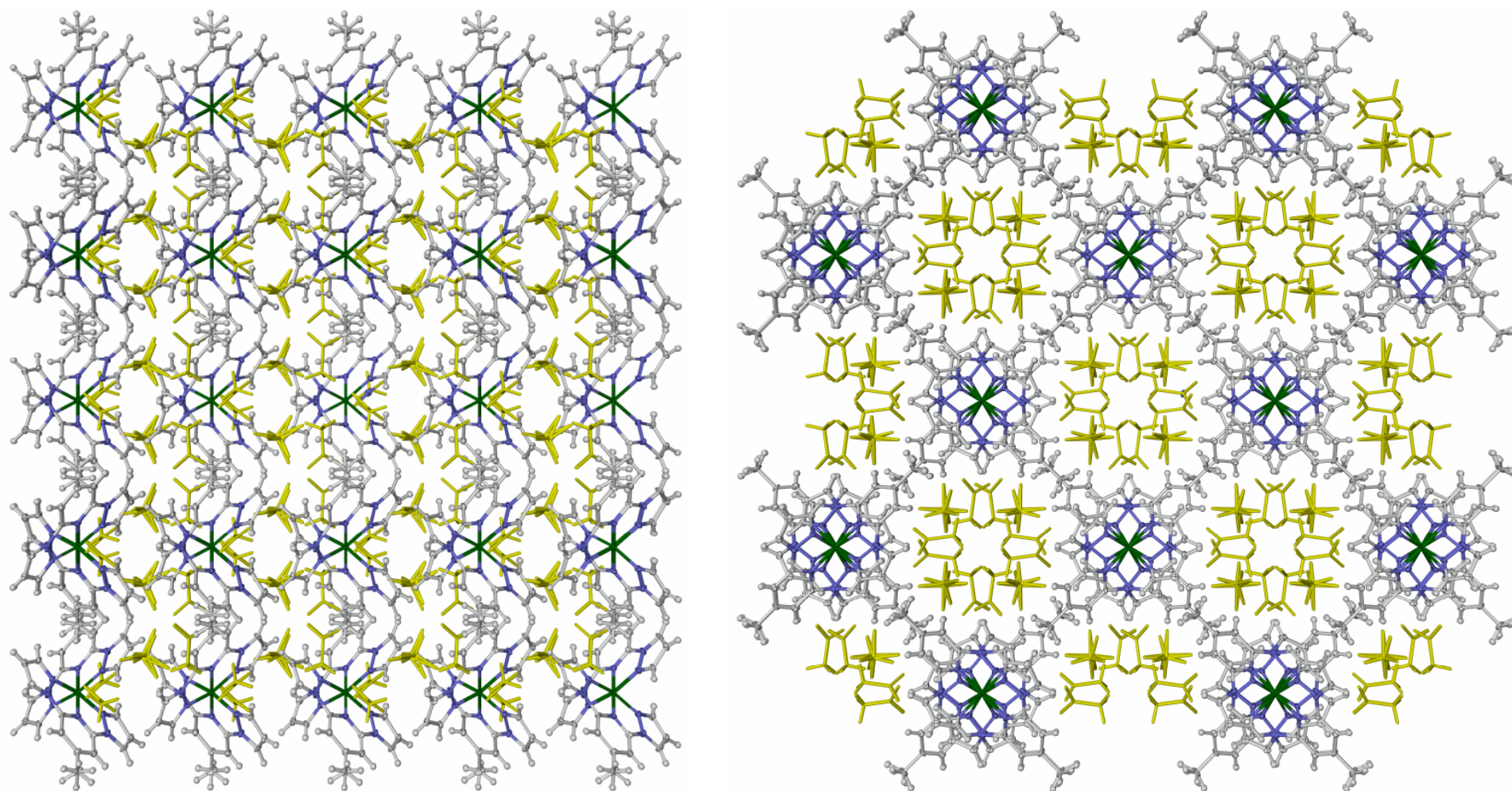


Figure S1 Two views of the packing diagram of $1 \cdot 4\text{MeNO}_2$, showing the channels of anions and solvent running parallel to c . The views are perpendicular to the (100) (left) and (001) (right) crystal planes. The atoms in the complex dication have 50 % displacement ellipsoids, while the anions and solvent are de-emphasized for clarity. Only one of the two disorder orientations of the unique nitromethane molecule is shown, but two disorder sites of the methyl H atoms and the BF_4^- ions (which both span crystallographic C_2 axes) have been generated by the program.

Color code: C{complex}, white; H{complex}, pale grey; N{complex}, blue; Fe, green; BF_4^- and CH_3NO_2 , yellow.

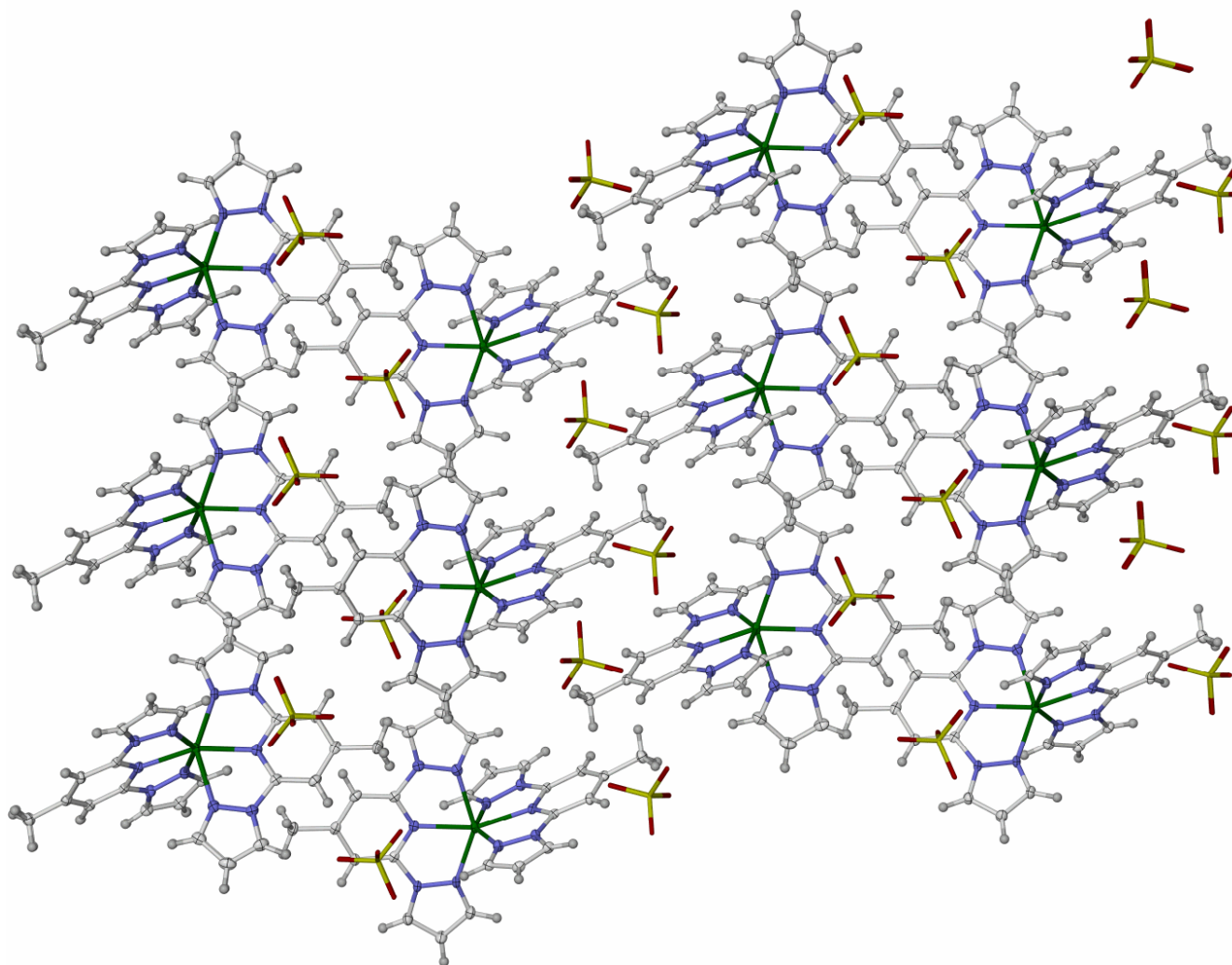


Figure S2 Packing diagram of **2**, showing a side-on view of the terpyridine embrace layers in the lattice. The view is perpendicular to the (010) plane, with *c* horizontal. An alternative view of this crystal packing is in Figure 3 of the main article.

Table S3 Metric parameters for the intermolecular π - π interactions in the terpyridine embrace layers in **2** (Å, °). See Figs. 2 and 3 of the main article. Symmetry codes: (v) $x, 1+y, z$; (vi) $-1+x, y, z$.

	Dihedral angle	Interplanar distance	Horizontal offset
<i>T</i> = 100 K			
[N(8)–C(12)]...[N(13 ^v)–C(17 ^v)]	5.92(15)	3.358(9)	1.65
[N(25)–C(29)]...[N(30 ^{vi})–C(34 ^{vi})]	8.07(13)	3.451(7)	1.15
<i>T</i> = 240 K			
[N(8)–C(12)]...[N(13 ^v)–C(17 ^v)]	5.9(6)	3.45(3)	1.65
[N(25)–C(29)]...[N(30 ^{vi})–C(34 ^{vi})]	4.9(5)	3.49(3)	1.34

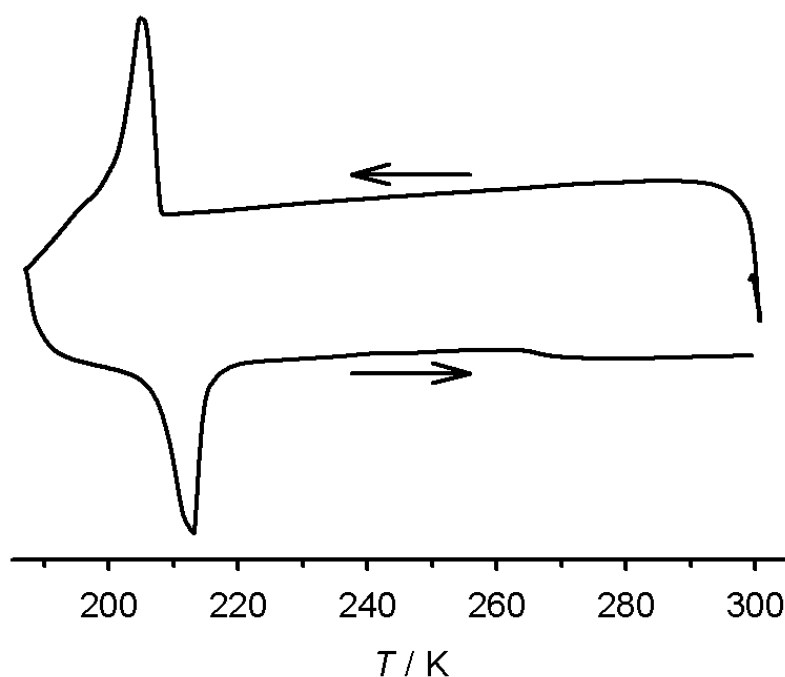


Figure S3 Differential scanning calorimetry (DSC) trace of **1** showing its abrupt, hysteretic spin-transition. The temperature ramp was 5 K min⁻¹.

A similar scan of **2** was featureless, because its spin-transition temperature in cooling mode ($T_{1/2\downarrow} = 175$ K) is below the minimum temperature accessible with this calorimeter (185 K).

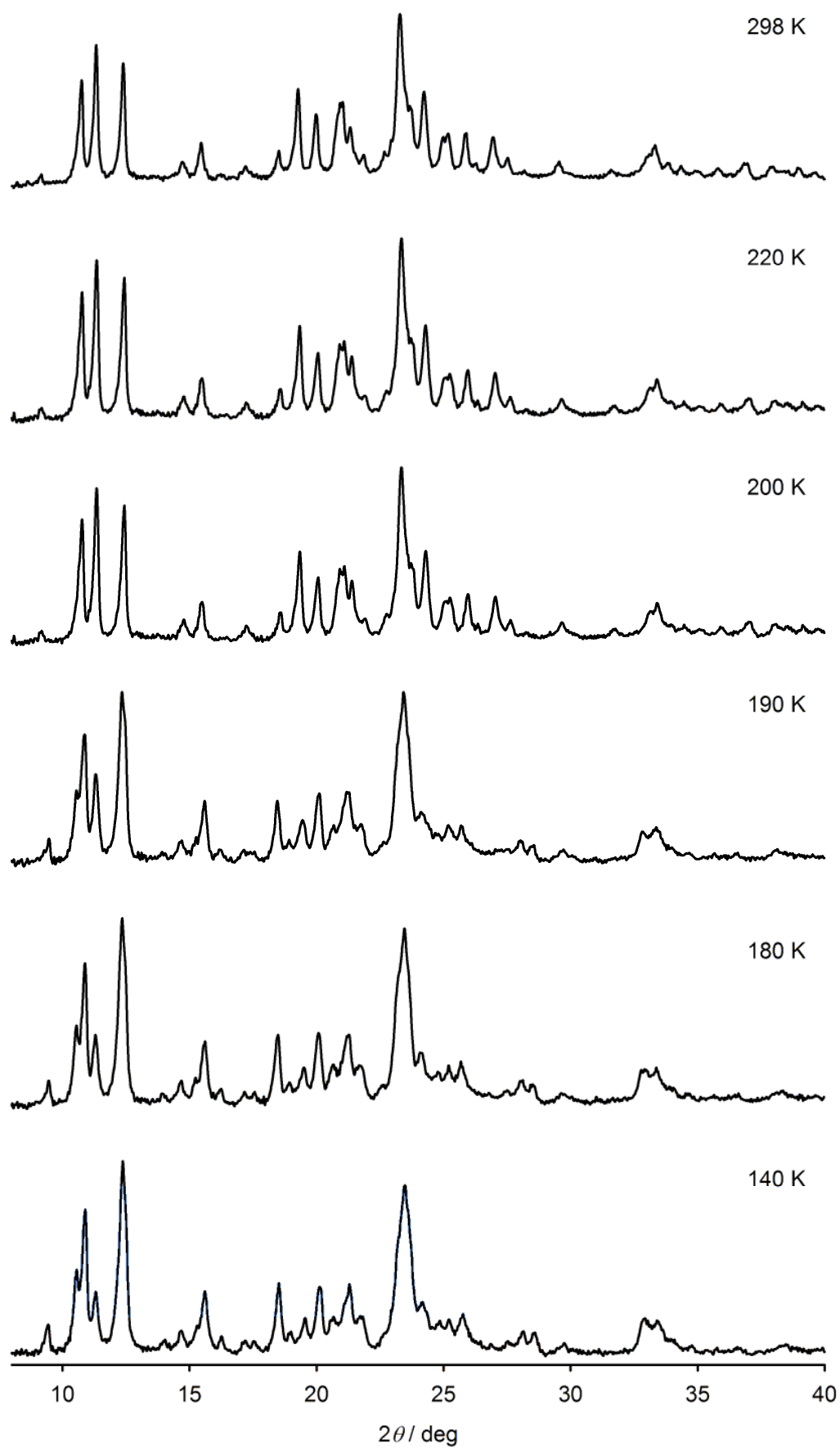


Figure S4 Variable temperature X-ray powder patterns from **1** at 10-20 Torr pressure. The data are the same as in Fig. 5 of the main article.

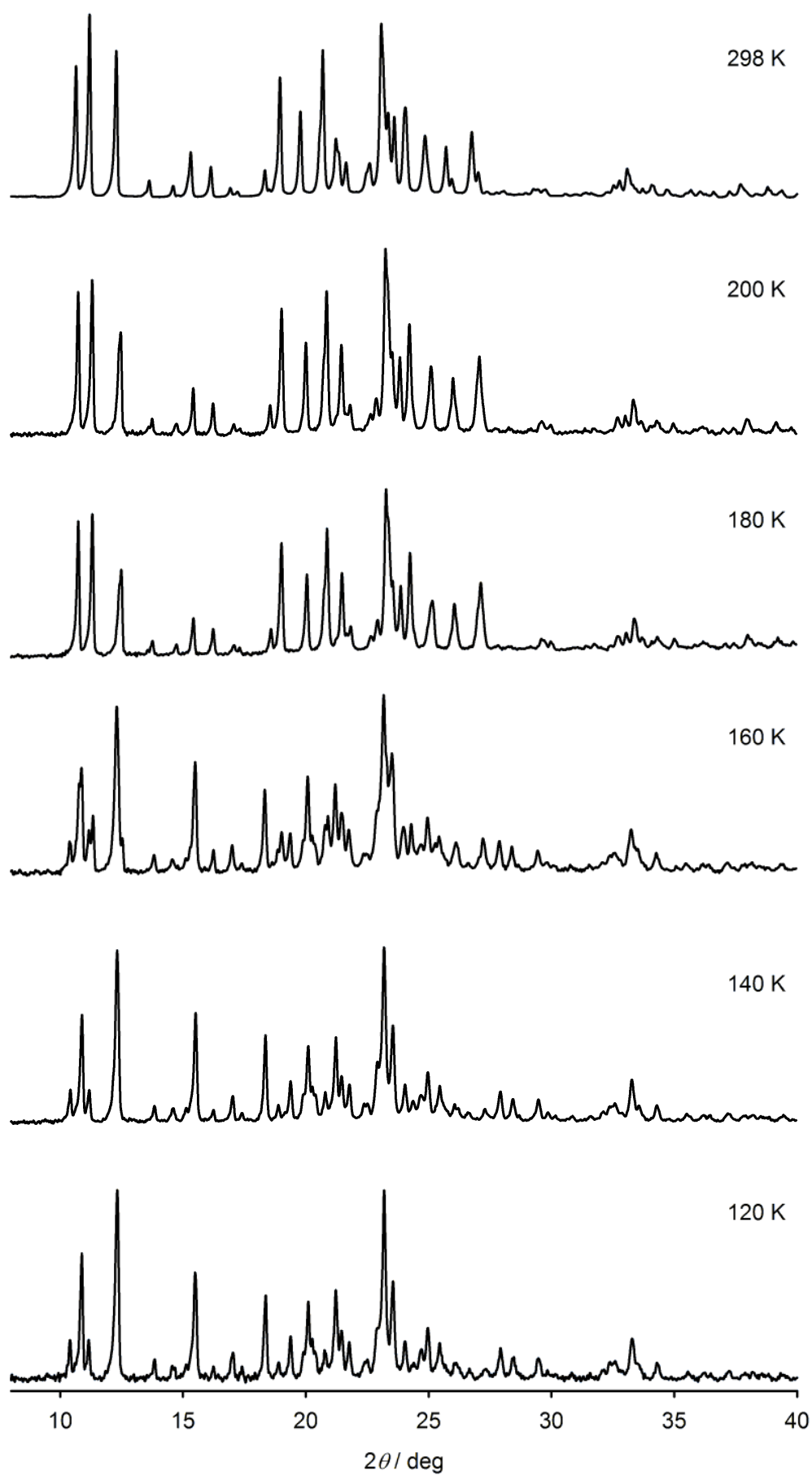


Figure S5 Variable temperature X-ray powder patterns from **2** at 10-20 Torr pressure. The data are the same as in Fig. 5 of the main article. At 160 K, the sample contains a mixture of the high- and low-temperature phases, showing that the phase transition is in progress at this temperature.

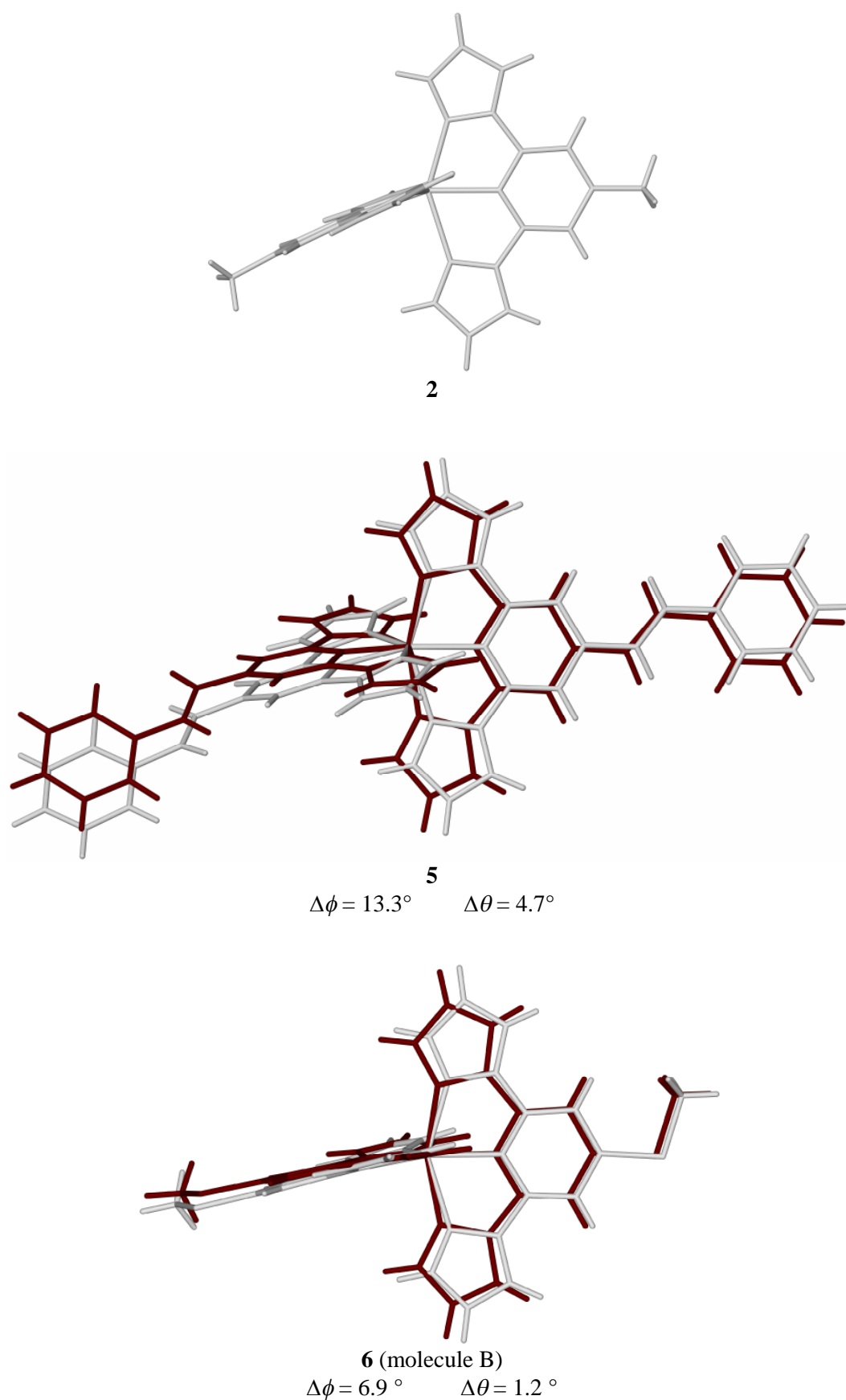


Figure S6 Comparison of the high-spin structure of **2**, with the overlaid high-spin (white) and low-spin (red) molecular structures of **5**⁵ and **6**.⁶

Although its low-spin form was not crystallographically characterized, comparable molecular structure changes are also likely during spin-crossover of **2** which would contribute to its thermal hysteresis.

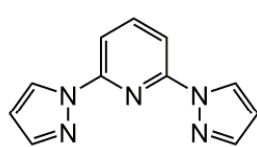
Table S4 Structural changes taking place during spin-crossover for $[\text{Fe}(\text{1-bpp})_2]^{2+}$ and its derivatives, whose high-spin and low-spin crystal structures are available. See above, and Chart 1 of the main article, for the definitions of ϕ , θ , Σ and Θ . The ligands referred to in the Table are shown in Chart S1 (next page). This is an updated version of the corresponding tables in refs. 3 and 4.

	$T_{1/2}$ (K)	$\Delta T_{1/2}$ (K) ^a	$\Delta\phi$ (°)	$\Delta\theta$ (°)	$\Delta\Sigma$ (°)	$\Delta\Theta$ (°)	Ref.
$[\text{FeL}_2][\text{ClO}_4]_2$ (2)	184	18	–	–	–	–	This work
$[\text{Fe}(L^1)_2][\text{BF}_4]_2 \cdot (\text{CH}_3)_2\text{CO}$ (5)	172	15	13.3	4.7	73.1	216	5
$[\text{Fe}(L^2)_2][\text{BF}_4]_2$ (6), molecule B [molecule A]	269 [≈ 270]	2 [g]	6.9 [0.0 ^b]	1.2 [1.0 ^b]	64.3 [50.2 ^b]	186 [141 ^b]	6
$[\text{Fe}(\text{1-bpp})_2][\text{BF}_4]_2$	260	3	5.2	0.5	64.7	185	7
$[\text{Fe}(\text{1-bpp})_2][\text{Ni}(\text{mnt})_2]_2 \cdot \text{CH}_3\text{NO}_2$	170	0-70 ^c	0.5	4.5	63.8	168	8
$[\text{Fe}(\text{1-bppy})_2][\text{BF}_4]_2 \cdot 3\text{CH}_3\text{NO}_2$	198	a ^d	4.2	0.18	62.1	180	9
$[\text{Fe}(L^3)_2][\text{ClO}_4]_2$	233	3	4.2	0.14	70	192	10
$[\text{Fe}(L^4)_2][\text{BF}_4]_2$	202	3	3.1	0.18	67.8	190	11
$[\text{Fe}(L^5)_2][\text{BF}_4]_2$	147	6 ^e	3.4	5.5	60.2	177	12
$[\text{Fe}(L^5)_2][\text{ClO}_4]_2$	267	vg	1.0 ^b	0.2 ^b	50.2 ^b	153 ^b	13
$[\text{Fe}(L^6)_2][\text{BF}_4]_2$	235	g, g ^f	0	0	56.3	151	9, 14
$[\text{Fe}(L^6)_2][\text{ClO}_4]_2$	196	a, g ^f	0	0	60.0	164	9, 14
$[\text{Fe}(L^7)_2][\text{BF}_4]_2$	271	g	1.13	0.16	56.4	157	10, 15
$[\text{Fe}(L^7)_2][\text{ClO}_4]_2$	284	g	0.3	0.62	54	152	10
β - $[\text{Fe}(L^8)_2][\text{BF}_4]_2$	272	g	5.9	0.2	60.0	173	16
$[\text{Fe}(L^9)_2][\text{BF}_4]_2$	307	g	1.3	0.04	63.2	176	6
$[\text{Fe}(L^{10})_2][\text{BF}_4]_2$	341	8	5.3 ^g	5.52 ^g	74.1 ^g	200 ^g	17

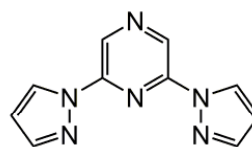
^aa = abrupt, no hysteresis; g = gradual; vg = very gradual. ^bmay be slightly under-estimated, since either a fully low-spin or fully high-spin crystal structure was not achieved. ^cStructured hysteresis loop. ^dAbrupt spin-transition from crystallographic measurements, but the presence of hysteresis was not determined. ^eFirst step of a two-stage spin-crossover, involving a re-entrant symmetry breaking phase transition. The second step occurs sluggishly, to the extent that its temperature could not be accurately determined. ^fTwo step transition from a single iron site, with a discontinuity at 50 % conversion. ^gCompound undergoes a phase change during spin-crossover, with one unique molecule in the high-spin phase and two unique molecules in the low-spin phase. Values given are the averaged values across the two low-spin molecules.

The parameter that correlates most strongly with the observation of spin-crossover hysteresis in these compounds is $\Delta\theta$.

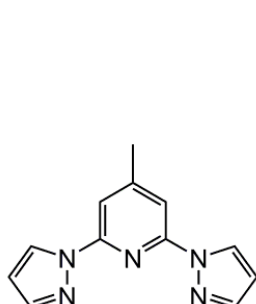
Chart S1 Ligands referred to in Table S4.



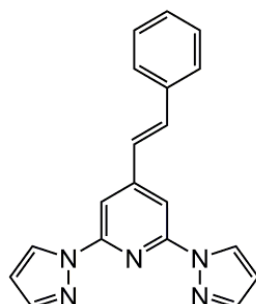
1-bpp



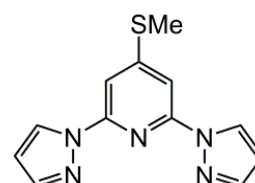
1-bppyz



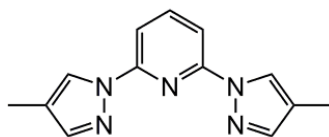
L



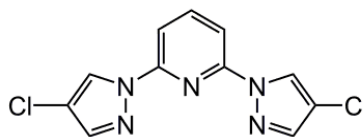
L^1



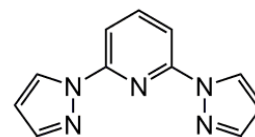
L^2



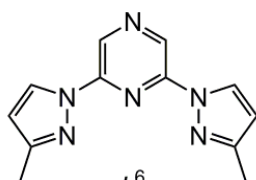
L^3



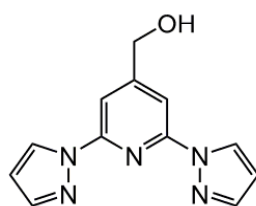
L^4



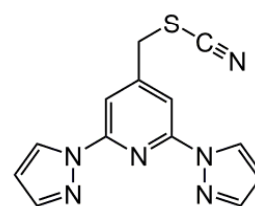
L^5



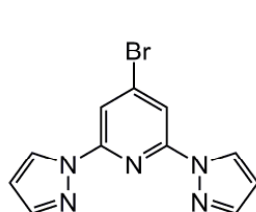
L^6



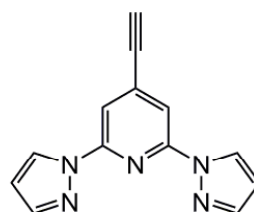
L^7



L^8



L^9



L^{10}

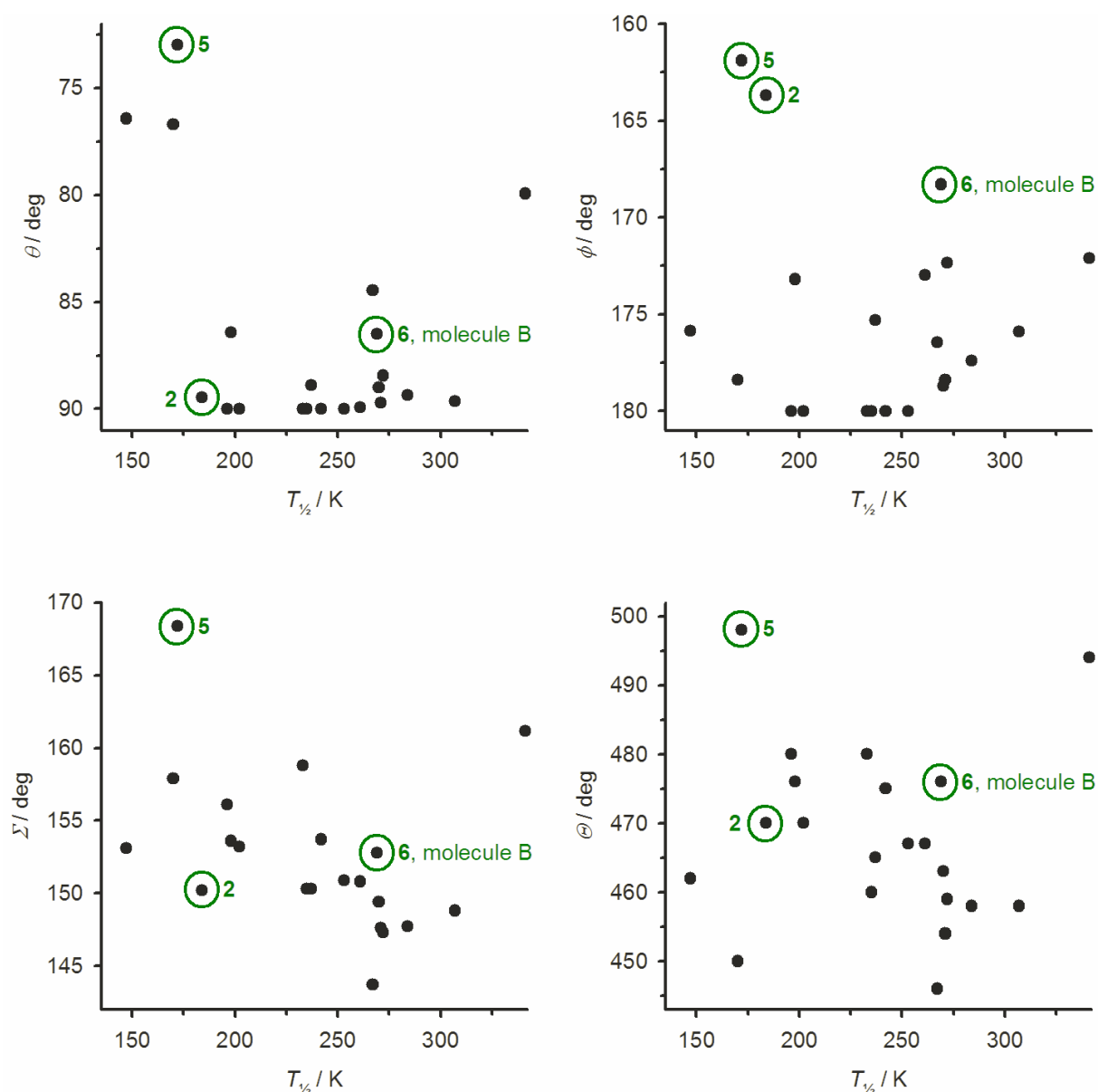


Figure S7 Plots of $T_{1/2}$ for solid $[\text{Fe}(\text{1-bpp})_2]^{2+}$ derivatives against the distortion parameters θ , ϕ , Σ and Θ of the high-spin state of the complexes. Data are taken from refs. 3-6 and 15-19.

Definitions of θ and ϕ are in Chart 1 of the main article, while Σ and Θ are defined at the beginning of this Supporting Information document. The graphs are each plotted so that the y axis indicates an increasing structural distortion.

A literature study of complexes of type $[\text{Fe}(\text{NCS})_2\text{L}_2]$ (L = a bidentate N-donor ligand) found a good linear relationship between $T_{1/2}$ and a parameter related to Θ .²⁰ The graphs for Σ vs. $T_{1/2}$ and Θ vs. $T_{1/2}$ may indicate a similar relationship in the main body of the data, although there are a lot of outliers. [Σ and Θ are strongly correlated in $[\text{Fe}(\text{1-bpp})_2]^{2+}$ complexes when $\Theta < \text{ca. } 500^\circ$].²

A more detailed experimental and computational study of this question, taking into account perturbations of $T_{1/2}$ caused by the inductive properties of ligand substituents in the different compounds, is in progress.

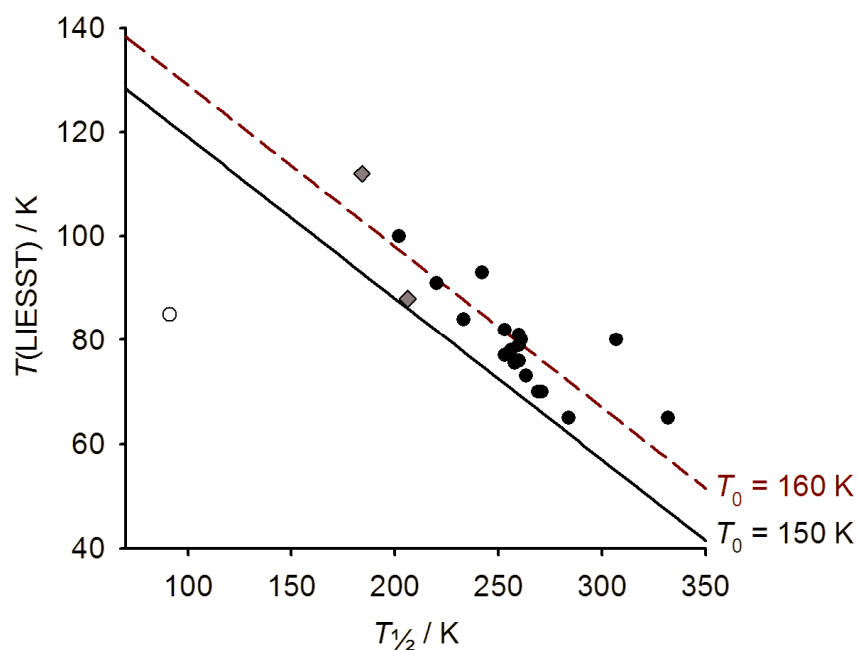


Figure S8 Relationship between $T_{1/2}$ and $T(\text{LIESST})$ for compounds from the $[\text{Fe}(\text{1-bpp})_2]^{2+}$ series, measured by these authors.^{4,6,10,12,18,19,21}

Gray diamonds: **1** and **2** (this work).

Black circles: previously published compounds that show an inverse relationship between $T_{1/2}$ and $T(\text{LIESST})$.

White circle: one previously published compound that deviates strongly from the relationship, reflecting some unique structural chemistry related to its particularly low $T_{1/2}$ value.¹²

The previously proposed empirical relationship between these parameters, $T_{1/2} = T_0 - 0.3T(\text{LIESST})$ with $T_0 = 150 \text{ K}$, is shown as a black solid line.^{10,23} A modified correlation with $T_0 = 160 \text{ K}$ (red dashed line) in fact fits these data more closely (the $T_0 = 150 \text{ K}$ relationship was originally formulated based on other compounds with a closely related, but different, ligand type).²²

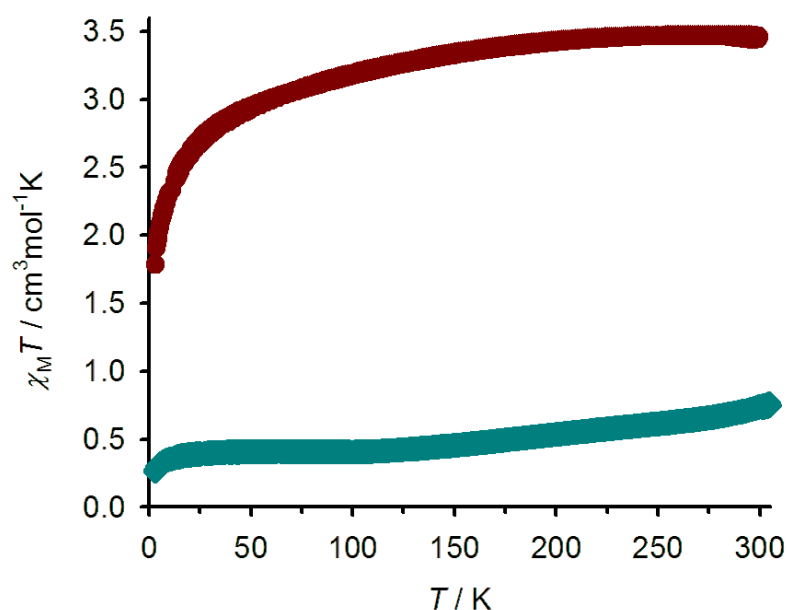


Figure S9 Variable temperature magnetic susceptibility data for **3** (red) and **4**·½H₂O (cyan).

Solid **3** is high-spin over the complete temperature range, which is consistent with its crystal structure. The decrease in $\chi_M T$ at low temperatures reflects zero-field splitting of the high-spin centers, and is not related to spin-crossover.

Compound **4**·½H₂O is *ca.* 80 % low-spin at room temperature, with a very gradual spin-equilibrium occurring upon cooling. Around 10 % of this material remains frozen in its high-spin state below 100 K, with a small zero-field splitting feature below 50 K as above.

References

- (1) McCusker, J. K.; Rheingold, A. L.; Hendrickson, D. N. *Inorg. Chem.* **1996**, *35*, 2100–2112.
- (2) Guionneau, P.; Marchivie, M.; Bravic, G.; Létard, J.-F.; Chasseau, D. *Top. Curr. Chem.* **2004**, *234*, 97–128.
- (3) Halcrow, M. A. *Chem. Soc. Rev.* **2011**, *40*, 4119–4142.
- (4) Halcrow, M. A. *Coord. Chem. Rev.* **2009**, *253*, 2493–2514.
- (5) Hasegawa, Y.; Sakamoto, R.; Takahashi, K.; Nishihara, H. *Inorg. Chem.* **2013**, *52*, 1658–1665.
- (6) Kershaw Cook, L. J.; Shepherd, H. J.; Comyn, T. P.; Baldé, C.; Cespedes, O.; Chastanet, G.; Halcrow, M. A. *Chem. Eur. J.* **2015**, *21*, 4805–4816.
- (7) Holland, J. M.; McAllister, J. A.; Lu, Z.; Kilner, C. A.; Thornton-Pett, M.; Halcrow, M. A. *Chem. Commun.*, **2001**, 577–578.
- (8) Nihei, M.; Tahira, H.; Takahashi, N.; Otake, Y.; Yamamura, Y.; Saito, K.; Oshio, H. *J. Am. Chem. Soc.* **2010**, *132*, 3553–3560.
- (9) Elhaïk, J.; Money, V. A.; Barrett, S. A.; Kilner, C. A.; Evans, I. R.; Halcrow, M. A. *Dalton Trans.* **2003**, 2053–2060.
- (10) Carbonera, C.; Costa, J. S.; Money, V. A.; Elhaïk, J.; Howard, J. A. K.; Halcrow, M. A.; Létard, J.-F. *Dalton Trans.* **2006**, 3058–3066.
- (11) Pritchard, R.; Kilner, C. A.; Halcrow, M. A. *Chem. Commun.* **2007**, 577–579.
- (12) Money, V. A.; Carbonera, C.; Elhaïk, J.; Halcrow, M. A.; Howard, J. A. K.; Létard, J.-F. *Chem. Eur. J.* **2007**, *13*, 5503–5514.
- (13) Elhaïk, J.; Kilner, C. A.; Halcrow, M. A. *Eur. J. Inorg. Chem.* **2014**, 4250–4253.
- (14) Money, V. A.; Elhaïk, J.; Evans, I. R.; Halcrow, M. A.; Howard, J.A.K. *Dalton Trans.* **2004**, 65–69.
- (15) Money, V. A.; Elhaïk, J.; Halcrow, M. A.; Howard, J.A.K. *Dalton Trans.* **2004**, 1516–1518.
- (16) Haryono, M.; Heinemann, F. W.; Petukhov, K.; Gieb, K.; Müller, P.; Grohmann, A. *Eur. J. Inorg. Chem.* **2009**, 2136–2143.
- (17) Šalitroš, I.; Fuhr, O.; Eichhöfer, A.; Kruk, R.; Pavlik, J.; Dlhán, L.; Boča, R.; Ruben, M. *Dalton Trans.* **2012**, *41*, 5163–5171.
- (18) Pritchard, R.; Lazar, H.; Barrett, S. A.; Kilner, C. A.; Asthana, S.; Carbonera, C.; Létard, J.-F.; Halcrow, M. A. *Dalton Trans.* **2009**, 6656–6666.
- (19) Mohammed, R.; Chastanet, G.; Tuna, F.; Malkin, T. L.; Barrett, S. A.; Kilner, C. A.; Létard, J.-F.; Halcrow, M. A. *Eur. J. Inorg. Chem.* **2013**, 819–831.
- (20) Marchivie, M.; Guionneau, P.; Létard, J.-F.; Chasseau, D. *Acta Cryst. Sect. B* **2005**, *61*, 25–28.
- (21) Chastanet, G.; Tovee, C. A.; Hyett, G.; Halcrow, M. A.; Létard, J.-F. *Dalton Trans.* **2012**, *41*, 4896–4902.
- (22) Marcen, S.; Lecren, L.; Capes, L.; Goodwin, H. A.; Létard, J.-F. *Chem. Phys. Lett.* **2002**, *358*, 87–95.